

Organic/inorganic anions coupling enabled reversible high-valent redox in vanadium-based polyanionic compound

Huangxu Li^{a,b}, Chaohong Guan^d, Ming Xu^{c,*}, Jun Guo^e, Kuo Yuan^b, Ke Cheng^b, Yangyang Xie^a, Liuyun Zhang^a, Jingqiang Zheng^a, Yanqing Lai^{a,*}, Zhian Zhang^{a,*}

^a School of Metallurgy and Environment, Engineering Research Center of the Ministry of Education for Advanced Battery Materials, Hunan Provincial Key Laboratory of Nonferrous Value-Added Metallurgy, Central South University, Changsha 410083, PR China

^b Department of Chemistry, City University of Hong Kong, Kowloon, Hong Kong 999077, PR China

^c School of Chemistry, Xi'an Jiaotong University, Xi'an 710049, PR China

^d University of Michigan–Shanghai Jiao Tong University Joint Institute, Shanghai Jiao Tong University, Shanghai 200240, PR China

^e School of Chemistry, Tiangong University, Tianjin 300387, PR China

ARTICLE INFO

Keywords:

Sodium-ion battery
Cathode
Vanadium-based
High energy
Polyanionic compound

ABSTRACT

Recently, there has been a drive to design and develop mixed polyanion compounds for positive electrode applications in sodium-ion batteries (SIBs) due to their high-valent redox, robust electrode framework and good safety. Although advances have been made, the exploration of new electrode materials and fundamental understanding of working mechanisms have been lacking. Here, we report a low-temperature synthesis of an organic/inorganic anions coupled $\text{Na}_2(\text{VO})_2(\text{HPO}_4)_2(\text{C}_2\text{O}_4)$ polyanionic compound (noted as NVPC), which exhibits a distinctive layered structure. The structure is able to stabilize reversible high-valent redox of $\text{V}^{4+}/^{5+}$, thereby the NVPC shows a moderate reversible capacity of 105 mA h g^{-1} at 0.1 C and a high redox potential around $4.00/3.80 \text{ V}$ vs. Na/Na^+ , which is larger than the NaVOPO_4 . The enhanced Na^+ diffusion capability and reduced band gap in NVPC is experimentally demonstrated by galvanostatic intermittent titration technique and theoretically validated by calculations. Besides, a small volume change (1.36%) of NVPC electrode during intercalation reaction is unambiguously demonstrated by diffraction and nanoscale structural analysis. Generally, our studies highlight that coupling organic/inorganic anions in polyanionic compounds is a practical strategy to stabilize high-valent redox center for developing high energy density SIB cathode materials.

1. Introduction

With the advent of large-scale power sources and electrified transportation, there is a pressing demand for cutting the full cost of energy storage devices, especially the current Li-ion battery technology with raising concerns that Li turns into the geopolitical resources in the future [1–6]. Among the energy storage technologies foreseen to combat this imminent issue, sodium-ion battery (SIB) holds the greatest promise because of the abundant natural resources with even geographic distribution of sodium (Na) and well-understood electrochemical operation involving the Na^+ charge carriers [7–12]. A clear consensus has been reached that the energy-density ceiling placed on the positive electrode is a primary factor precluding the full-scale deployment of SIB technologies. Hence, demands for high energy density have driven researchers to push the limits of Na ions intercalation reactions for positive electrodes, seeking to cycle increasingly more Na ions and electrons with

increasingly high voltage hosts, typically polyanionic compounds [13–17]. Through comparative studies, vanadium-centered polyanionic compounds such as $\text{Na}_3\text{V}_2(\text{PO}_4)_2\text{F}_3$ ($\text{PO}_4\text{-F}$), $\text{Na}_3\text{V}(\text{PO}_3)_3\text{N}$ ($\text{PO}_3\text{-N}$), and $\text{Na}_7\text{V}_4(\text{P}_2\text{O}_7)_4\text{PO}_4$ ($\text{PO}_4\text{-P}_2\text{O}_7$) with mixed anionic groups are among the most promising positive electrode materials [5,18–22]. The presence of mixed anions in the polyanionic sublattice structure with strong covalency can stabilize the $\text{V}^{3+}/^{4+}$ redox, leading to moderate redox voltage and capacity. Meanwhile, the antibonding $\text{V}^{4+}/^{5+}$ state is expected to be achieved to further increase the operating voltage. However, reversible high-valent $\text{V}^{4+}/^{5+}$ is rarely reported in mixed polyanionic compounds.

Recently, the oxalate group, $(\text{C}_2\text{O}_4)^{2-}$, is found to be compatible with $(\text{SO}_4)^{2-}$ and $(\text{PO}_4)^{3-}$ due to their similar electronic inductive effect on the d-states of the transition metal ions [23,24]. In addition, due to its exceptional conjugate base properties and small molecular weight (87.98) compared to $(\text{P}_2\text{O}_7)^{4-}$ (173.87), $(\text{SO}_4)^{2-}$ (96.02) and $(\text{PO}_4)^{3-}$ (94.93), the oxalate group have remained a versatile electrode

* Corresponding authors.

E-mail addresses: xuming@xjtu.edu.cn (M. Xu), laiyanqing@csu.edu.cn (Y. Lai), zhangzhian@csu.edu.cn (Z. Zhang).

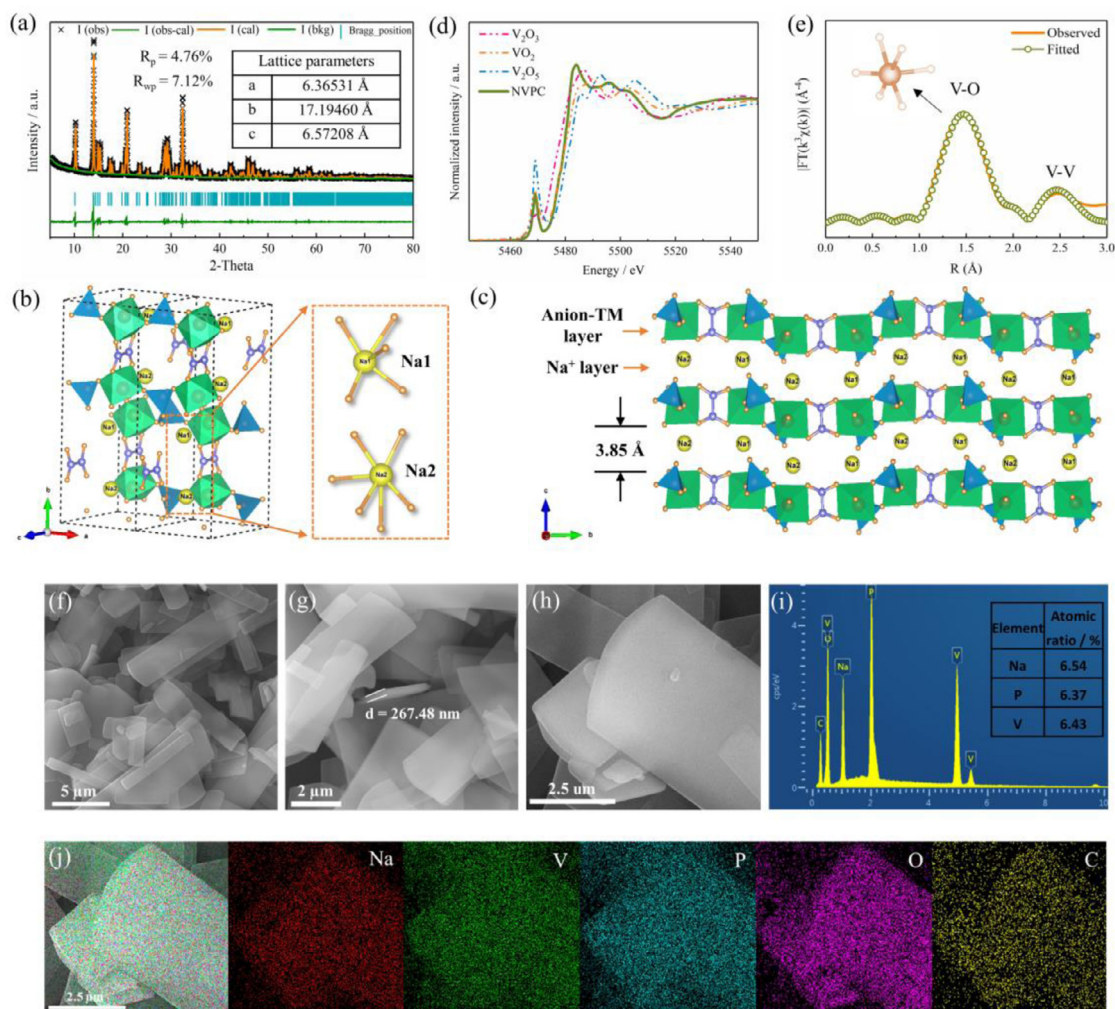


Fig. 1. Crystal structure and morphology of the NVPC material. (a) Rietveld refinement of the XRD pattern and cell parameters of NVPC. (b) Schematic illustration of the crystal structure of NVPC with two different Na sites. (c) Illustration of the layered structure of the organic/inorganic anions coupled framework. (d) XANES and (e) EXAFS of the NVPC. (f) SEM images of the NVPC at low and (g) high magnifications. (h) Electron image of the NVPC collected for Energy dispersive spectrometer (EDS) analysis. (i) EDS of NVPC. (j) Elemental mapping images of Na, V, P, O, and C in NVPC.

chemistry of choice that can lead to rich structural diversity and multiple electron redox activity [25,26]. So far, only $\text{Fe}^{2+/3+}$ redox centered oxalate-phosphate compounds were reported for SIB, [23,27,28] and the exploration of new electrode materials with high-valent redox center and fundamental understanding of working mechanisms have been lacking. Herein, we demonstrate that the high-valent $\text{V}^{4+/5+}$ redox center can be stabilized by coupling the $(\text{C}_2\text{O}_4)^{2-}$ anion group with $(\text{HPO}_4)^{2-}$ polyanionic sublattice structure. To achieve this aim, we have synthesized a polyanions mixed vanadium-based sodium oxalate-phosphate compound, formulated $\text{Na}_2(\text{VO})_2(\text{HPO}_4)_2(\text{C}_2\text{O}_4)$ (noted as NVPC) by a low-temperature hydrothermal method. Structural characterization using X-ray diffraction (XRD), Raman spectroscopy and high-resolution transmission electron microscopy (HRTEM) reveal that the NVPC compound has layered crystal structure and shows a small volume change of only 1.36% during intercalation reaction. In addition, with the aid of density functional theories (DFT) and galvanostatic intermittent titration technique (GITT), it is shown that the high Na^+ reversibility and robust electrode structure are associated with the $(\text{C}_2\text{O}_4)^{2-}$ and $(\text{HPO}_4)^{2-}$ coupling and the resulted small forbidden band gap, and low energy barrier 2D Na^+ ion migration paths. Our findings indicate that coupling the oxalate group with polyanions provides a viable strategy to stabilize high-voltage redox in the polyanionic compound and thus is promising to rejuvenate the research field of positive electrode of SIB.

2. Results and discussion

The NVPC materials were obtained by hydrothermal method, followed by vacuum drying at 150 °C to eliminate crystal water in the structure. XRD pattern shows that the crystal phase of NVPC has no significant changes during the drying process (Fig. S1). Further detailed crystal structure of NVPC was analyzed by Rietveld refinement. As shown in Fig. 1a, the NVPC was revealed to adopt a single-phase monoclinic structure with space group of $P2_1$. No impurities are observed. The lattice parameters are determined to $a = 6.36531$ Å, $b = 17.19460$ Å, $c = 6.57208$ Å and $V = 689.28$ Å³. Occupation information of the atoms are listed in Table S1, and crystal structure of the material is depicted in Figs. 1b, 1c and S2. In the crystal structure of NVPC, there are two different Na sites: the Na1 and Na2 site, which are coordinated by five and six oxygen atoms, respectively. Vanadium octahedra is connected with PO_4H tetrahedron by corner-sharing to form $[\text{VOHPO}_4]$ infinite chains along a-axis direction. The $[\text{VOHPO}_4]$ chains are then linked by (C_2O_4) groups along b-axis direction, leading to $[(\text{VO})_2(\text{HPO}_4)_2(\text{C}_2\text{O}_4)]$ anion-TM layers with layered spacing of 3.85 Å. Na1 and Na2 reside in the space between the anion-TM layers alternatively. Such layered structure is rarely seen in conventional polyanionic compounds, which generally show 3D frameworks structure [16]. X-ray absorption spectroscopy (XAS) was conducted to examine the local circumstance of

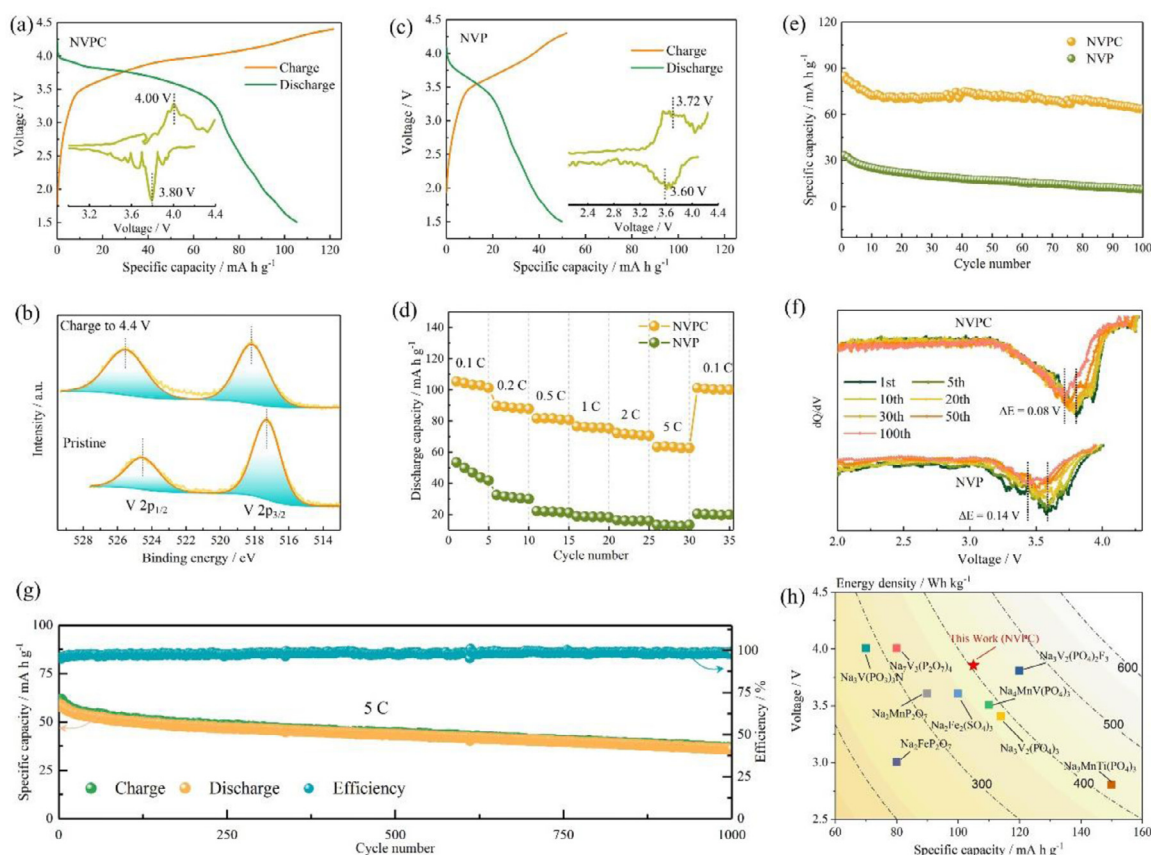


Fig. 2. Electrochemical performances of the materials. Galvanostatic charge/discharge curves and their corresponding dQ/dV patterns of (a) NVPC and (c) NVP. (b) XPS of NVPC electrode at pristine and charged to 4.4 V states. (d) Rate performance of NVPC and NVP. (e) Cycling stability at 0.2 C. (f) dQ/dV plots of different cycles of NVPC and NVP at 0.2 C. (g) Long cycling stability of the NVPC at high rate of 5 C. (h) Comparison between the NVPC material and other cathode materials reported in terms of redox potential, energy density, and specific capacity [5,34–41].

V. X-ray absorption near-edge structure (XANES) signals of NVPC and V_2O_3 , VO_2 and V_2O_5 are presented in Fig. 1d. The pre-edge of NVPC is mostly overlapped with that of VO_2 , indicating that the valence state of V is close to +4 in NVPC. The extended X-ray absorption fine structure (EXAFS) is shown in Fig. 1e. Fitting process was conducted under k^3 -weight conditions to obtain bonding information. The peak at around 1.5 Å can be assigned to V–O bonds, and V is coordinated with 6 oxygens to form VO_6 octahedra. While the peak at around 2.5 Å is V–V bonds, which derive from the interaction of adjacent VO_6 octahedra. X-ray photoelectron spectroscopy (XPS) was employed to examine chemical composition and bonding structure of the material. The full survey identifies the composition of Na, V, P, C, O elements in the material (Fig. S3a). The V 2p_{3/2} and V 2p_{1/2} peaks are located at 517.24 eV and 524.59 eV, respectively, indicating the valence state of V is +4 (Fig. S3b) [29,30]. For C 1 s, the peaks at 286.54 eV and 288.99 correspond to C–O band and C=O band, respectively, which should derive from the (C₂O₄) groups (Fig. S3c) [29,31]. The O 1 s further confirmed the bonding structure of O–C band (531.29 eV) and O=C band (532.59 eV, Fig. S3d). Thermostability of the material was determined by Thermogravimetric test. It shows that the polyanions mixed material starts to decompose at around 330 °C (Fig. S4). Morphology and structure of the NVPC was further studied by scanning electron microscopy (SEM). It shows a long-board like shape with a wide length distribution that mainly ranges from 2 μm to 20 μm (Fig. 1f), and the thickness of the longboard is around 267.48 nm (Fig. 1g). Energy-dispersive X-ray spectroscopy (EDS) mapping of NVPC are presented in Fig. 1h–j. It demonstrates that Na, V, P, O, C are evenly distributed in the NVPC plates. The atomic ratio of Na: P: V was determined to be 6.54%: 6.37%: 6.43%, which is close to the theoretical ratio (1:1:1). The theoretical carbon content should be

5.22 wt.% according to the formula of NVPC, and the carbon content in NVPC was quantified to be 5.18 wt.% by elemental analysis (C/S). These results confirm high purity of the material.

The NVPC material with a layered crystal structure is attractive to be applied as a cathode material for SIBs. To this end, the materials were subjected to galvanostatic operation within the voltage window of 1.5 ~ 4.4 V (vs. Na⁺/Na). As shown in Fig. 2a, the NVPC exhibits a moderate charge and discharge capacity of 121.5 and 105.4 mA h g^{−1}, respectively, at 0.1 C (1C = 100 mA g^{−1}). Galvanostatic charge/discharge curves demonstrate that redox potential of the NVPC is around 4.00/3.80 V, which is confirmed by the dQ/dV plots (inset). *Ex-situ* XPS was employed to clarify the origin of the high voltage. As shown in Fig. 2b, the peaks of V 2p_{3/2} and V 2p_{1/2} in the pristine electrode shift from 517.29 to 524.58 eV to high values of 518.18 and 525.53 respectively when the electrode was charged to 4.4 V, indicating that the high-valent redox of V⁴⁺/V⁵⁺ couple is realized in NVPC [32]. To show the impact of anions coupling on structure and electrochemical properties of electrode materials, the NaVOPO₄ material (NVP) which has been well-studied to show a 3D tunneled structure and the same V⁴⁺/V⁵⁺ redox was synthesized for comparison [33]. XRD confirms the successful synthesis of monoclinic (S.G. P2₁/c) NVP with high purity (Fig. S5). Morphology of the NVP particles is presented in Fig. S6. It shows that the NVP delivers a limited discharge capacity of 49.9 mA h g^{−1} at 0.1 C and redox potential of 3.72/3.60 V as indicated by the dQ/dV plots (Fig. 2c). CV curves further confirms that the NVPC possesses higher redox potential (Fig. S7), which should be derived from the accumulated inductive effect of mixed anions Fig. 2d shows rate performance of NVPC and NVP. It demonstrates that capacity of the NVP drastically decreases to below 20 mA h g^{−1} when the current density

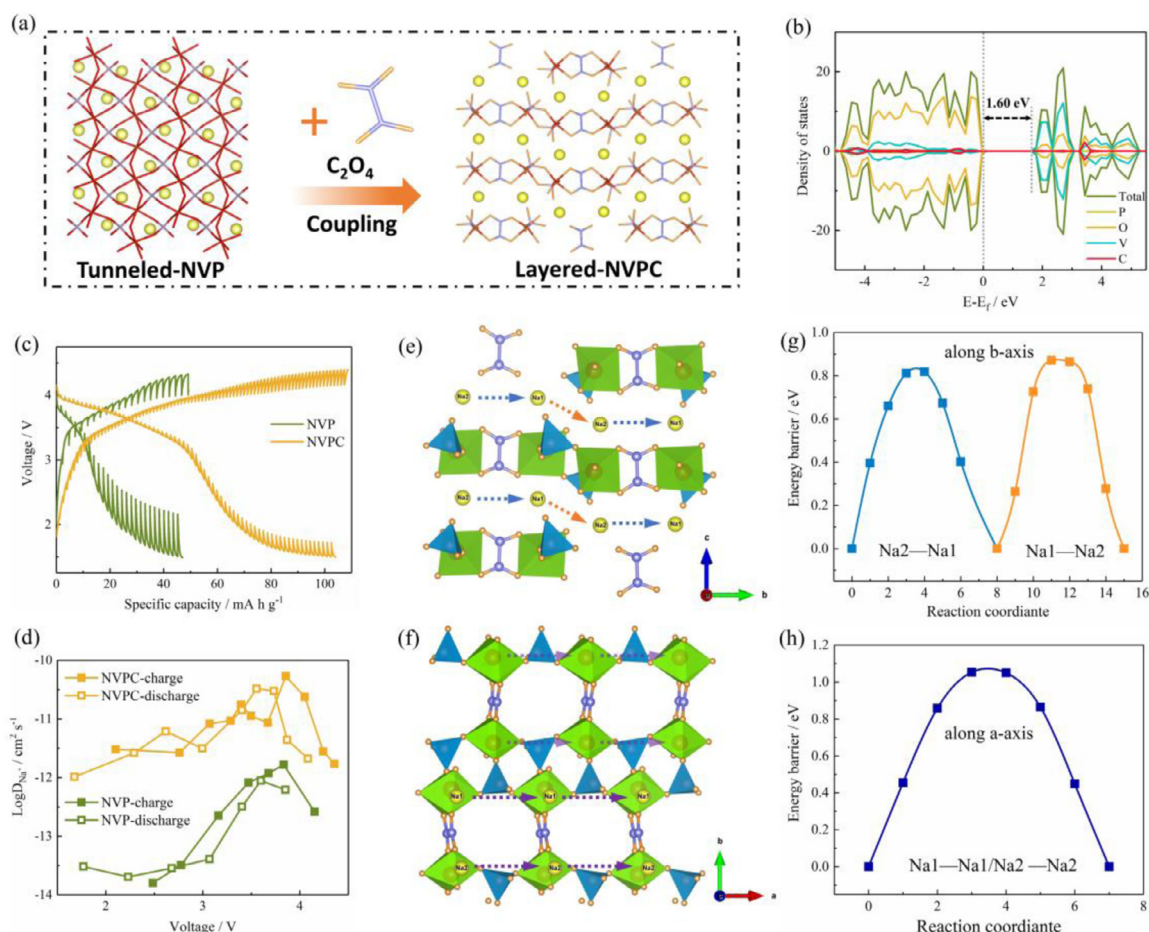


Fig. 3. Sodium storage kinetics of the materials. (a) Schematic illustration of the crystal structure differences between NVP and NVPC. (b) DOS of the NVPC. (c) GITT profiles and (d) Na-diffusion coefficients of NVPC and NVP electrodes. Schematic illustrations of sodium-ion diffusion path along (e) b-axis and (f) a-axis. (g) Energy barriers of sodium-ion migration following Na2–Na1 and Na1–Na2 patterns along b-axis. (i) Energy barriers of sodium-ion migration following Na1–Na1 and Na2–Na2 patterns along a-axis.

increases from 0.1 C to above 1 C. At the high rate of 5 C, the NVP only delivers a discharge capacity of 13.3 mA h g^{-1} . When the current turns back from 5 C to 0.1 C, only 20.5 mA h g^{-1} of discharge capacity can be maintained, indicating poor reversibility of the NVP. In the contrast, reversibility of the NVPC is good. It is able to display a discharge capacity of 105.4, 89.7, 81.6, 76.5, 72.2, 63.4 mA h g^{-1} at 0.1, 0.2, 0.5, 1, 2, 5 C, respectively. When the current turns back from 5 C to 0.1 C, the discharge capacity recovers to $101.2 \text{ mA h g}^{-1}$. The corresponding discharge profiles of NVP and NVPC are depicted in Figs. S8 and S9. Cycling stability of the materials was also studied. After 100 cycles at 0.2 C, NVPC and NVP show a capacity retention of 74.7% and 33.8%, respectively (Fig. 2e). The corresponded dQ/dV curves of different cycles are depicted in Fig. 2f. A large redox voltage decrease of 0.14 V was found in NVP after 100 cycles. While, the voltage decay is mitigated in NVPC electrode, with only 0.08 V. Therefore, the enhanced cycling stability of NVPC should be ascribed to the stable high-valent redox reaction. The long cycling stability of NVPC at 5 C was further studied and a capacity retention of 61.2% after 1000 cycles was obtained (Fig. 2g). To evaluate the high-valent redox material, electrochemical performance of NVPC and some typical polyanionic compounds that reported were compared in terms of capacity, voltage, and energy density [5,34–41]. As presented in Fig. 2h, the V^{4+}/V^{5+} redox provides a high voltage and moderate capacity, making the NVPC a promising cathode material with high energy density.

Although both NVP and NVPC show V^{4+}/V^{5+} redox, their sodium storage performances are very different. This should be associated with

their crystal structures and the related reaction kinetics. As illustrated in Fig. 3a, the NVP shows a 3D-tunneled structure as many general polyanionic compounds do, while the incorporation of $(C_2O_4)^{2-}$ anion leads NVPC to form a layered structure. The calculated density of states (DOS) reveals a forbidden band gap of 1.60 eV in NVPC (Fig. 3b), which is smaller than that of the monoclinic NVP (2.03 eV) [42] and many other polyanionic compounds, such as $Na_3V_2(PO_4)_3$ (2.57 eV) [43] and $Na_3V_2(PO_4)_2F_3$ (2.75 eV) [44]. The reduced band gap is beneficial to electron transport in NVPC. Reaction kinetics of the electrodes were further studied by GITT. Fig. 3c is the quasi-open circuit potential profiles, based on which the D_{Na} of NVPC and NVP materials were calculated (Fig. S10). It shows that the D_{Na} for NVPC is mainly within the range of $10^{-10} \sim 10^{-11} \text{ cm}^2 \text{ s}^{-1}$ which is higher than that of NVP ($10^{-11} \sim 10^{-13} \text{ cm}^2 \text{ s}^{-1}$, Fig. 3d). The facile sodium diffusion should be related to the anions mixed framework with layered structure. To verify this, the DFT calculations were employed to disclose sodium-ion diffusion paths. Because the Na-ions are located in the interlayer spacing of anion-TM layers along ab-plane, the energy barrier could be very high for Na-ions pass across the anion-TM layers. Therefore, Na-ions migration within the ab-plane was studied. Fig. 3e and 3f illustrate the Na-ions migration along the b-axis and a-axis, respectively. The energy barrier for Na2–Na1 and Na1–Na2 migration paths along b-axis is 0.82 and 0.85 eV, respectively (Fig. 3g). For Na1–Na1/Na2–Na2 migration paths along a-axis, the energy barrier is 1.04 eV (Fig. 3h). Therefore, the anions coupled structure with reduced band gap, increased sodium ion diffusion capa-

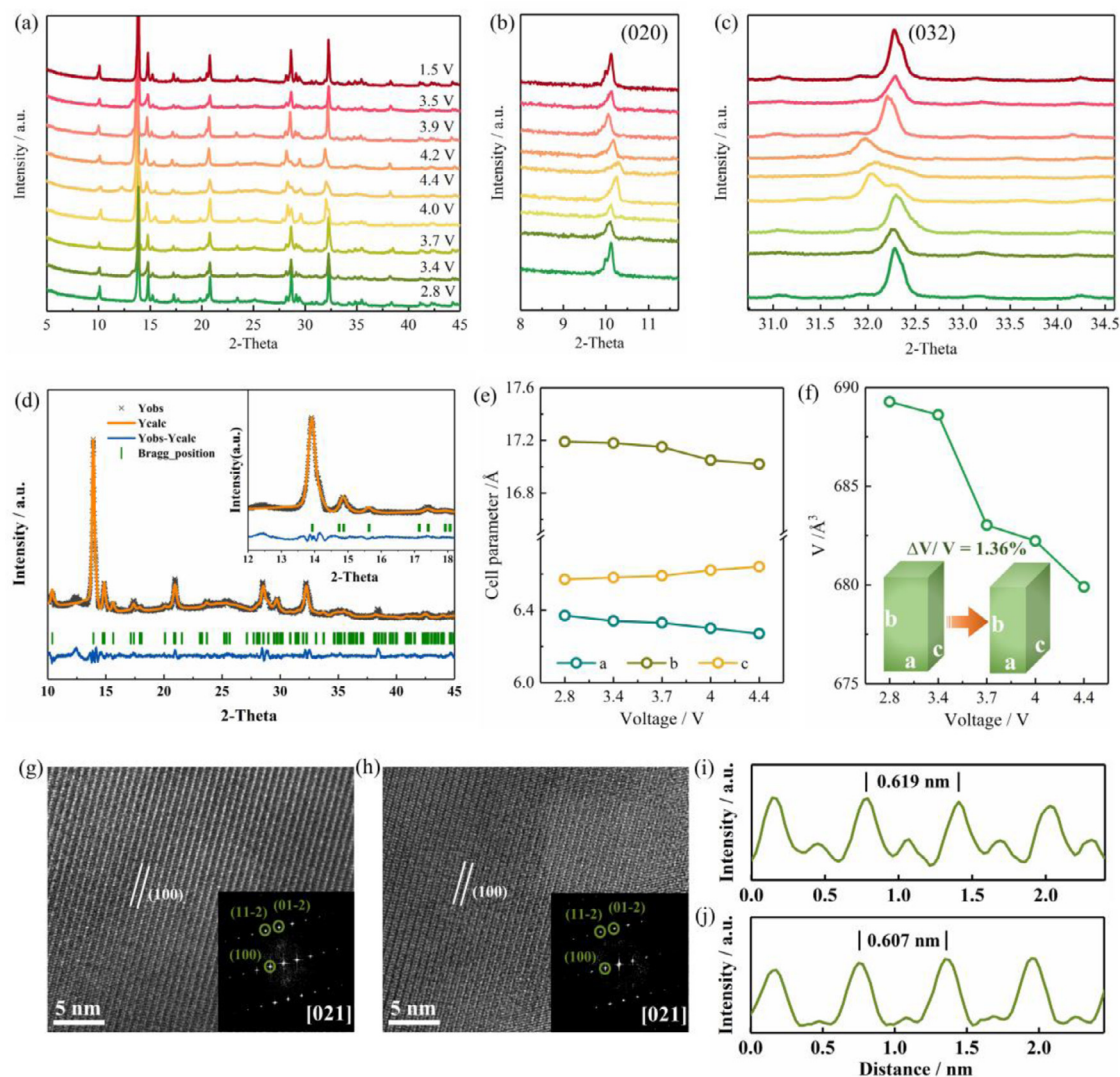


Fig. 4. Characterizations of sodium storage mechanism of the mixed polyanion materials. (a) *Ex-situ* XRD patterns of the NVPC electrode under different charge/discharge states and (b, c) the enlarged patterns at different partial ranges. (d) Rietveld refinement of the XRD pattern of the fully charged electrode. Inset shows the details of the fitting results. (e) Cell parameter changes and (f) volume changes of the material. (g) The HR-TEM and the corresponded FFT pattern of the pristine NVPC. (h) The HR-TEM and the corresponded FFT pattern of the NVPC electrode charged to 4.4 V. (i) Integrated pixel intensities collected from g. (j) Integrated pixel intensities collected from h.

bility, and 2D diffusion paths with small energy barriers are key to the facile sodium storage properties of NVPC.

The sodium storage mechanism and structural evolution of the layered material was primarily studied by *ex-situ* XRD. The XRD patterns of NVPC electrodes at different charge/discharge states were shown in Fig. 4a–c. A clearly continuous peak shift of the (020) reflection can be seen in Fig. 4b, manifesting an intercalation/deintercalation mechanism accompany with lattice parameter changes during sodium extraction/insertion [45]. Besides, the peak variation modes in the 2-theta region of $31.5^\circ \sim 33^\circ$ suggest a two-phase reaction mechanism of the material. Specifically, the peak of (032) reflection in Fig. 4c was found left shift firstly when charging to 3.7 V, and then it splits into two peaks when further charged to above 4.0 V. The emergence of new peaks indicates a phase transition process. To disclose the phase transition, Rietveld refinement of the XRD of the fully charged electrode was conducted. As presented in Fig. 4d, the fitting results are satisfactory, with a $R_p = 4.13$ and $R_{wp} = 5.77$. Details of the atomic position are listed in Table S3. It shows that full Na^+ extraction leads to a Na-free $(\text{VO})_2(\text{HPO}_4)_2(\text{C}_2\text{O}_4)$ phase (noted as VPC), which also adopts a monoclinic $P2_1$ crystal phase. The crystal phase is the same to the pristine

NVPC. Therefore, the phase transition from NVPC to VPC is quite similar to the well-investigated phase transition from O3 to O3' in layered oxide materials, in which their crystal phases are the same and the peaks variation among the two end members is believed to associate with the content of Na^+ , valence of transition metals, as well as their local environments in the host structure [46]. Note that, during the discharge process, all the peaks recover to their initial positions, meaning that the lattice framework evolution is highly reversible (Fig. 4a–c). Rietveld refinement was also conducted on XRD of the electrodes at 3.4 V, 3.7 V and 4.4 V (Fig. S11–13 and Table S4–6). Lattice parameter changes of the materials are then analyzed by and presented in Fig. 4e and f. Lattice changes in NVPC before and after charge process were detected by HR-TEM. As shown in Fig. 4g and h, FFT patterns of the two samples are both along the [021] zone, indicating that the lattice displays the same facets in the two samples. The (100) facet with a lattice spacing of 0.619 nm (Fig. 4i) can be identified. When fully charged to 4.4 V, the lattice spacing of (100) facet decreases to 0.607 nm (Fig. 4j), verifying that the lattice shrinkage is accompanied with sodium extraction in the charge process. The volume change between NVPC and VPC phase was calculated to be merely 1.36% (Fig. 4f). The small volume change mani-

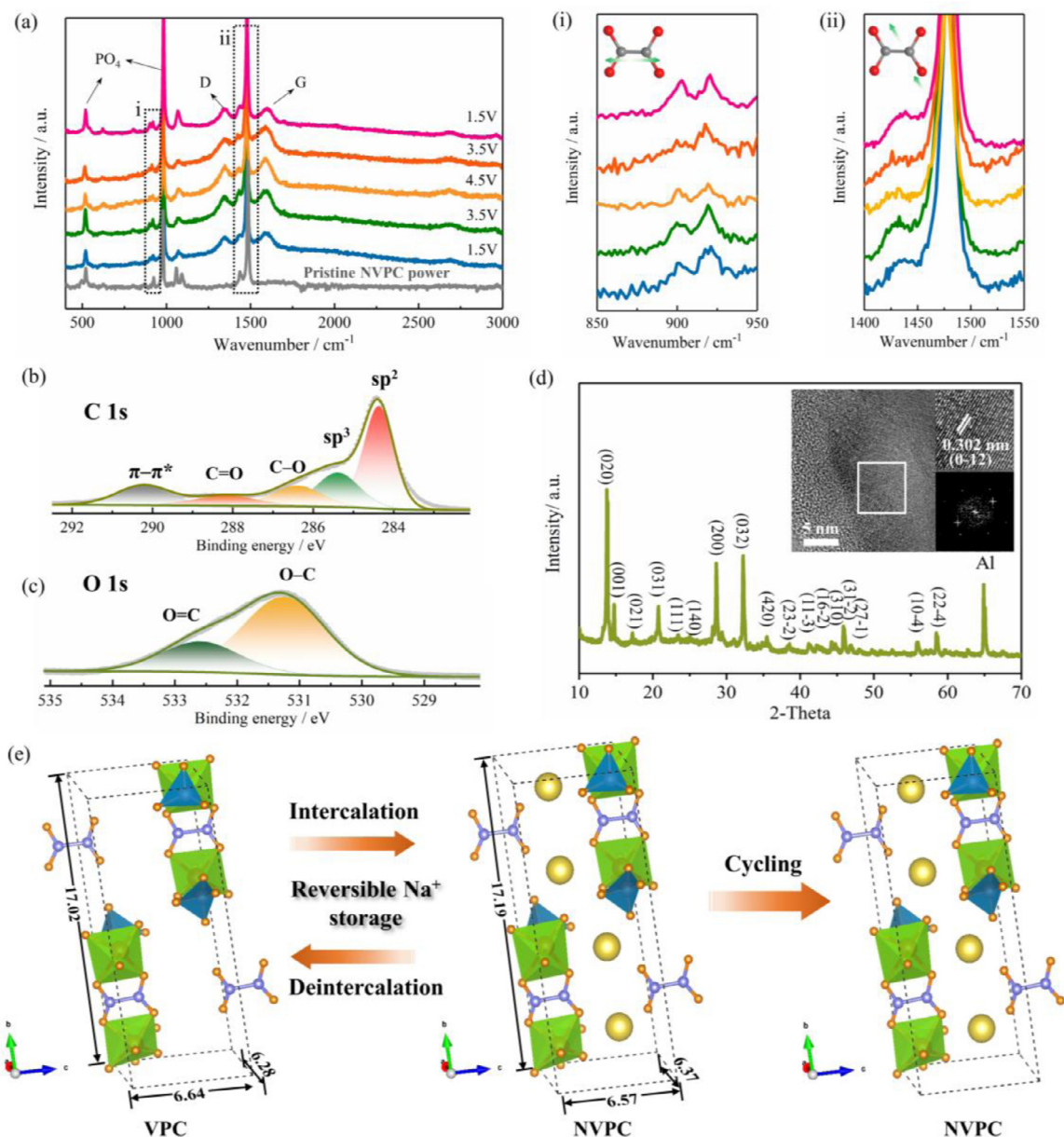


Fig. 5. Characterizations of the stability of polyanions mixed framework during sodium storage. (a) *Ex-situ* Raman patterns of the NVPC electrodes. (i, ii) The enlarged Raman patterns that showing two different vibration modes of $(C_2O_4)^{2-}$ groups. (b) XPS spectra of C 1s and (c) O1s of the NVPC electrode after 1000 cycles at 5 C. (d) The XRD patterns of NVPC electrodes after 1000 cycles at 5 C. The insets are HR-TEM images of the NVPC electrode after the long cycling, enlarged image showing the lattice, and the corresponded FFT pattern. (e) Schematic illustration of the sodium storage mechanism and stability of the layered framework.

feats that low strain was caused during sodium intercalation/extraction, which is beneficial for cycling stability of the material.

For polyanionic compounds, because the oxygen atoms are stabilized by strong covalent bonds in the polyanion groups, so polyanionic compounds do not show oxygen release and have good structural stability [14,47]. Nevertheless, the stable frameworks of polyanionic compounds in previous literature are generally composed of inorganic polyanions. The impact of organic species on stability of polyanionic compounds is rarely understood. Therefore, the stability of organic (C_2O_4) polyanion group in the mixed polyanion framework should be taken into consideration. *Ex-situ* Raman was then employed (Fig. 5a). The peaks at 518.7 and 987.8 cm^{-1} can be indexed to the vibration of (PO_4) group, and peaks at 1344.8 and 1591.5 cm^{-1} correspond to the D-band (disordered carbon) and G-band (graphitized carbon), respectively [35]. The regions that contain vibration signal of (C_2O_4) group were highlighted in Fig. 5a and further enlarged. The peaks in region i (850–950 cm^{-1}) and region

ii (1400–1550 cm^{-1}) correspond to the symmetric stretching mode of C–C and asymmetric stretching mode of C=O, respectively [26]. It shows that the peaks of both C–C symmetric stretching and asymmetric C=O stretching are stable at different charge/discharge states. Even at the charge state of 4.4 V, no significant changes have been observed comparing to the origin electrode at 1.5 V. These results imply that the (C_2O_4) groups are stable during the sodium extraction/insertion process. Stability of the organic group in the framework during long cycling were further studied by XPS. As shown in Fig. 5b, the peaks of C–O band (286.48 eV) and C=O band (288.38 eV) that derive from the (C_2O_4) groups can be detected [29,31]. Besides, the bonding structure of O–C band (531.24 eV) and O=C band (532.61 eV) in the O 1s spectra was also identified (Fig. 5c), indicating that the (C_2O_4) groups is stable to afford long cycling. Crystal structure of NVPC electrode after 1000 cycles at 5 C was checked by XRD. All peaks can be indexed to the NVPC phase (Fig. 5d). Microstructure of the cycled electrode was checked by

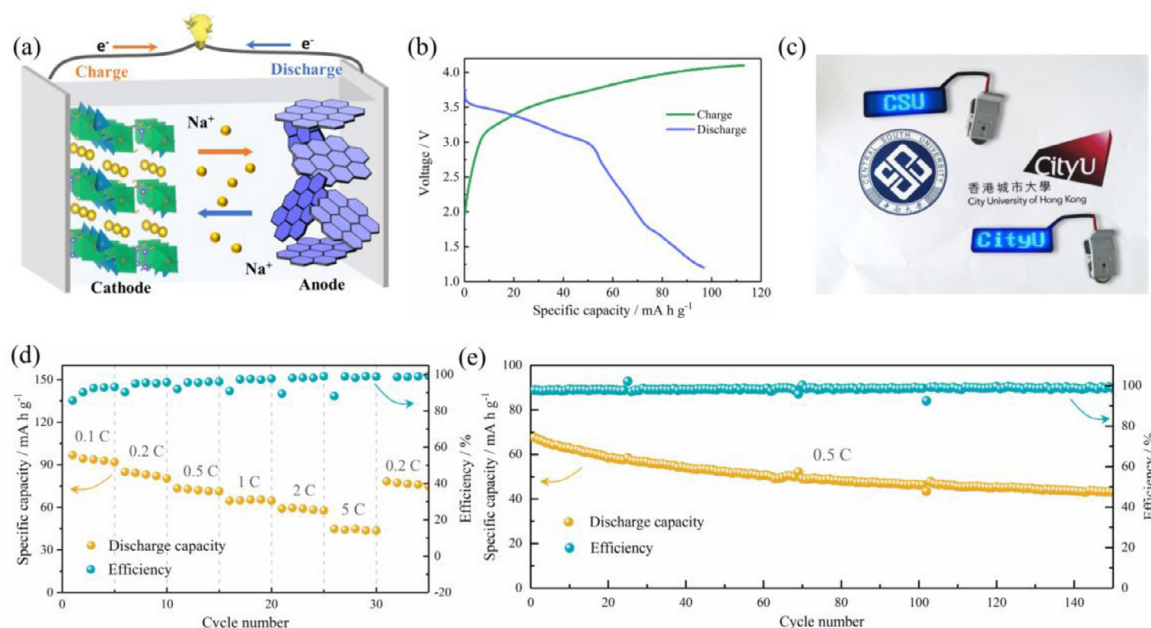


Fig. 6. Electrochemical performance of the NVPC//HC full cells. (a) Illustration of the configuration of the full cell. (b) Charge/discharge curves of the NVPC//HC full cell at 0.1 C. (c) Picture of LED badges powered by the full cells. (d) Rate performance and (e) cycling stability of the full cells.

HR-TEM, and the (0–12) facet of monoclinic NVPC with a lattice spacing of 0.302 nm was detected. These results indicate that crystal framework of the material maintains well. Therefore, during the sodium storage process, the organic/inorganic coupled layered framework is reversible and also robust, which is key to the durability of the NVPC material. Based on crystal structure analysis, structure evolution of the NVPC material is illustrated in Fig. 5e and a reversible sodium storage mechanism in the layered structure is presented. Both of the Na1 and Na2 are electrochemically active for energy storage. The highly reversible Na-intercalation/deintercalation with low strain is critically important to the high performance of NVPC.

To evaluate practical application possibility of the NVPC material, hard carbon (HC) anodes were used to help assemble full cells. The configuration of the full cell is illustrated in Fig. 6a. The HC is able to deliver a reversible capacity of 253.9 mA h g⁻¹ at current density of 50 mA g⁻¹ (Fig. S14). To avoid large capacity penalty that results from the low Coulombic efficiency of HC, the electrodes were run for 20 cycles in half cells initially to obtain a stable state (Fig. S15). As a result, the assembled NVPC//HC full cells demonstrate a high charge/discharge capacity of 112.6/96.7 mA h g⁻¹ (based on the cathode) at 0.1 C within the voltage window of 1.2–4.1 V (Fig. 6b). The full cell is able to offer power for LED badges (Fig. 6c). Rate performance and cycling stability of the full cell are also studied. A discharge capacity of 94.3, 85.0, 73.4, 64.6, 59.1 and 44.8 mA h g⁻¹ at 0.1, 0.2, 0.5, 1, 2, and 5 C, respectively, was obtained (Fig. 6d). The full cell also demonstrates acceptable cycling stability, with a capacity retention of 64.1% after 150 cycles at 0.5 C (Fig. 6e).

3. Conclusions

To summarize, the organic/inorganic anions coupled Na₂(VO)₂(HPO₄)₂(C₂O₄) material with distinctive layered structure was synthesized and applied as a cathode material for SIBs. The reversible high-valent redox of V⁴⁺/V⁵⁺ endows the NVPC electrode a high redox potential of 4.0/3.8 V and a considerable reversible capacity of 105.4 mA h g⁻¹. The anions coupling structure also leads to enhanced reaction kinetics in NVPC due to the reduced band gap and high sodium diffusion coefficients. A highly reversible sodium deintercalation/intercalation mechanism with a small volume change of

1.36% in the layered structure was identified, and the robust structure with small volume change is key to the good cycling stability of NVPC. This work not only provides a new polyanionic compound for SIB, but also deepens understanding about the properties of organic/inorganic anion coupling framework for materials design and energy storage.

Declaration of Competing Interest

The authors declare no conflict of interest.

Data Availability

Data will be made available on request.

Acknowledgements

The authors thank the financial support from the National Natural Science Foundation of China (52104312), the Natural Science Foundation of Hunan Province, China (2020JJ1007) and the Anhui Province Research and Development Innovation Project for Automotive Power Battery Efficient Recycling System. The authors also thank the Shiyanjia Lab (www.shiyanjia.com) for XPS analysis.

Supplementary materials

Supplementary material associated with this article can be found, in the online version, at doi:10.1016/j.enstm.2022.02.044.

References

- [1] F. Duffner, N. Kronmeyer, J. Tübke, J. Leker, M. Winter, R. Schmich, Post-lithium-ion battery cell production and its compatibility with lithium-ion cell production infrastructure, *Nat. Energy* 6 (2021) 123–134.
- [2] Y. Liang, H. Dong, D. Aurbach, Y. Yao, Current status and future directions of multivalent metal-ion batteries, *Nat. Energy* 5 (2020) 646–656.
- [3] Y. Huang, Y. Zhu, H. Fu, M. Ou, C. Hu, S. Yu, Z. Hu, C. Chen, G. Jiang, H. Gu, H. Lin, W. Luo, Y. Huang, Mg-Pillared LiCoO₂: Towards Stable Cycling at 4.6 V, *Angew. Chem. Int. Ed.* 133 (2021) 4732–4738.
- [4] T. Cheng, Z. Ma, R. Qian, Y. Wang, Q. Cheng, Y. Lyu, A. Nie, B. Guo, Achieving Stable Cycling of LiCoO₂ at 4.6 V by Multilayer Surface Modification, *Adv. Funct. Mater.* 31 (2021) 2001974.

- [5] G. Liang, Z. Wu, C. Didier, W. Zhang, J. Cuan, B. Li, K. Ko, P. Huang, C. Lu, Y. Chen, G. Leniec, M. Kaczmarek, B. Johannessen, L. Thomsen, V.K. Peterson, W. Pang, Z. Guo, A Long Cycle-Life High-Voltage Spinel Lithium-Ion Battery Electrode Achieved by Site-Selective Doping, *Angew. Chem. Int. Ed.* 59 (2020) 10594–10602.
- [6] G. Liang, V.K. Peterson, K. See, Z. Guo, W. Pang, Developing high-voltage spinel $\text{LiNi}_{0.5}\text{Mn}_{1.5}\text{O}_4$ cathodes for high-energy-density lithium-ion batteries: current achievements and future prospects, *J. Mater. Chem. A* 8 (2020) 15373–15398.
- [7] L. Jiang, L. Liu, J. Yue, Q. Zhang, A. Zhou, O. Borodin, L. Suo, H. Li, L. Chen, K. Xu, Y.S. Hu, High-Voltage Aqueous Na-Ion Battery Enabled by Inert-Cation-Assisted Water-in-Salt Electrolyte, *Adv. Mater.* 32 (2020) e1904427.
- [8] F. Gebert, D.L. Cortie, J.C. Bouwer, W. Wang, Z. Yan, S.X. Dou, S.L. Chou, Epitaxial Nickel Ferrocyanide Stabilizes Jahn-Teller Distortions of Manganese Ferrocyanide for Sodium-Ion Batteries, *Angew. Chem. Int. Ed.* 60 (2021) 18519–18526.
- [9] H. Li, W. Zhang, K. Sun, J. Guo, K. Yuan, J. Fu, T. Zhang, X. Zhang, H. Long, Z. Zhang, Y. Lai, H. Sun, Manganese-Based Materials for Rechargeable Batteries beyond Lithium-Ion, *Adv. Energy Mater.* 11 (2021) 2100867.
- [10] X. Xiang, K. Zhang, J. Chen, Recent Advances and Prospects of Cathode Materials for Sodium-Ion Batteries, *Adv. Mater.* 27 (2015) 5343–5364.
- [11] Y. You, A. Manthiram, Progress in High-Voltage Cathode Materials for Rechargeable Sodium-Ion Batteries, *Adv. Energy Mater.* 8 (2018) 1701785.
- [12] Y. You, S. Kim, A. Manthiram, A Honeycomb-Layered Oxide Cathode for Sodium-Ion Batteries with Suppressed P3–O1 Phase Transition, *Adv. Energy Mater.* 7 (2017) 1601698.
- [13] H. Li, M. Xu, Z. Zhang, Y. Lai, J. Ma, Engineering of Polyanion Type Cathode Materials for Sodium-Ion Batteries: Toward Higher Energy/Power Density, *Adv. Funct. Mater.* 30 (2020) 2000473.
- [14] Q. Ni, Y. Bai, F. Wu, C. Wu, Polyanion-Type Electrode Materials for Sodium-Ion Batteries, *Adv. Sci.* 4 (2017) 1600275.
- [15] P. Barpanda, L. Lander, S.I. Nishimura, A. Yamada, Polyanionic Insertion Materials for Sodium-Ion Batteries, *Adv. Energy Mater.* 8 (2018) 1703055.
- [16] T. Jin, H. Li, K. Zhu, P.F. Wang, P. Liu, L. Jiao, Polyanion-type cathode materials for sodium-ion batteries, *Chem. Soc. Rev.* 49 (2020) 2342–2377.
- [17] Y. Lan, W. Yao, X. He, T. Song, Y. Tang, Mixed Polyanionic Compounds as Positive Electrodes for Low-Cost Electrochemical Energy Storage, *Angew. Chem. Int. Ed.* 59 (2020) 9255–9262.
- [18] S.Y. Lim, H. Kim, J. Chung, J.H. Lee, B.G. Kim, J.J. Choi, K.Y. Chung, W. Cho, S.J. Kim, W.A. Goddard, Y. Jung, J.W. Choi, Role of intermediate phase for stable cycling of $\text{Na}_7\text{V}_4(\text{P}_2\text{O}_7)_4\text{PO}_4$ in sodium ion battery, *Proc. Natl. Acad. Sci. USA* 111 (2014) 599–604.
- [19] G. Yan, S. Mariyappan, G. Rousse, Q. Jacquet, M. Deschamps, R. David, B. Mirvaux, J.W. Freeland, J.M. Tarascon, Higher energy and safer sodium ion batteries via an electrochemically made disordered $\text{Na}_3\text{V}_2(\text{PO}_4)_2\text{F}_3$ material, *Nat. Commun.* 10 (2019) 585.
- [20] H. Yi, L. Lin, M. Ling, Z. Lv, R. Li, Q. Fu, H. Zhang, Q. Zheng, X. Li, Scalable and Economic Synthesis of High-Performance $\text{Na}_3\text{V}_2(\text{PO}_4)_2\text{F}_3$ by a Solvothermal–Ball-Milling Method, *ACS Energy Lett.* 4 (2019) 1565–1571.
- [21] Q. Li, B. Lin, S. Zhang, C. Deng, Towards high potential and ultra long-life cathodes for sodium ion batteries: freestanding 3D hybrid foams of $\text{Na}_7\text{V}_4(\text{P}_2\text{O}_7)_4(\text{PO}_4)$ and $\text{Na}_7\text{V}_3(\text{P}_2\text{O}_7)_4$ @biomass-derived porous carbon, *J. Mater. Chem. A* 4 (2016) 5719–5729.
- [22] J. Kim, G. Yoon, M.H. Lee, H. Kim, S. Lee, K. Kang, New 4V-Class and Zero-Strain Cathode Material for Na-Ion Batteries, *Chem. Mater.* 29 (2017) 7826–7832.
- [23] T. Song, W. Yao, P. Kiadkhunthod, Y. Zheng, N. Wu, X. Zhou, S. Tunmee, S. Sattayaporn, Y. Tang, A Low-Cost and Environmentally Friendly Mixed Polyanionic Cathode for Sodium-Ion Storage, *Angew. Chem. Int. Ed.* 132 (2019) 750–755.
- [24] M. Nagarathinam, K. Saravanan, E.J. Phua, M.V. Reddy, B.V. Chowdari, J.J. Vittal, Redox-active metal-centered oxalate phosphate open framework cathode materials for lithium ion batteries, *Angew. Chem. Int. Ed.* 51 (2012) 5866–5870.
- [25] W. Yao, L. Clark, M. Xia, T. Li, S.L. Lee, P. Lightfoot, Diverse Family of Layered Frustrated Magnets with Tailorable Interlayer Interactions, *Chem. Mater.* 29 (2017) 6616–6620.
- [26] W. Yao, A.R. Armstrong, X. Zhou, M.T. Sougrati, P. Kidkhunthod, S. Tunmee, C. Sun, S. Sattayaporn, P. Lightfoot, B. Ji, C. Jiang, N. Wu, Y. Tang, H.M. Cheng, An oxalate cathode for lithium ion batteries with combined cationic and polyanionic redox, *Nat. Commun.* 10 (2019) 3483.
- [27] W. Yao, M.T. Sougrati, K. Hoang, J. Hui, P. Lightfoot, A.R. Armstrong, $\text{Na}_2\text{Fe}(\text{C}_2\text{O}_4)_2\text{F}_2$: A New Iron-Based Polyoxoanion Cathode for Li/Na Ion Batteries, *Chem. Mater.* 29 (2017) 2167–2172.
- [28] W. Yao, M.T. Sougrati, K. Hoang, J. Hui, P. Lightfoot, A.R. Armstrong, Reinvestigation of $\text{Na}_2\text{Fe}_2(\text{C}_2\text{O}_4)_3\cdot 2\text{H}_2\text{O}$: An Iron-Based Positive Electrode for Secondary Batteries, *Chem. Mater.* 29 (2017) 9095–9101.
- [29] A.S. Hameed, M.V. Reddy, M. Nagarathinam, T. Runcevski, R.E. Dinnebier, S. Adams, B.V. Chowdari, J.J. Vittal, Room temperature large-scale synthesis of layered frameworks as low-cost 4 V cathode materials for lithium ion batteries, *Sci. Rep.* 5 (2015) 16270.
- [30] M.J. Aragón, P. Lavela, G.F. Ortiz, J.L. Tirado, Effect of Iron Substitution in the Electrochemical Performance of $\text{Na}_3\text{V}_2(\text{PO}_4)_3$ Cathode for Na-Ion Batteries, *J. Electrochem. Soc.* 162 (2015) A3077–A3083.
- [31] C. Gao, J. Li, K. Sun, H. Li, B. Hong, M. Bai, K. Zhang, Z. Zhang, Y. Lai, Controllable lithium deposition behavior hollow of N, O co-doped carbon nanospheres for practical lithium metal batteries, *Chem. Eng. J.* 412 (2021) 128721.
- [32] R. Klee, P. Lavela, M.J. Aragón, R. Alcántara, J.L. Tirado, Enhanced high-rate performance of manganese substituted $\text{Na}_3\text{V}_2(\text{PO}_4)_3/\text{C}$ as cathode for sodium-ion batteries, *J. Power Sources* 313 (2016) 73–80.
- [33] Z. Liang, R. Liu, Y. Xiang, J. Zhu, X. Liu, G.F. Ortiz, Y. Yang, Electrochemical investigation of multi-electron reactions in NaVOPO_4 cathode for sodium-ion batteries, *Electrochim. Acta* 351 (2020) 136454.
- [34] L.L. Zhang, D. Ma, T. Li, J. Liu, X.K. Ding, Y.H. Huang, X.L. Yang, Polypamine-Derived Nitrogen-Doped Carbon-Covered $\text{Na}_3\text{V}_2(\text{PO}_4)_2\text{F}_3$ Cathode Material for High-Performance Na-Ion Batteries, *ACS Appl. Mater. Interfaces* 10 (2018) 36851–36859.
- [35] Y. Fang, L. Xiao, X. Ai, Y. Cao, H. Yang, Hierarchical carbon framework wrapped $\text{Na}_3\text{V}_2(\text{PO}_4)_3$ as a superior high-rate and extended lifespan cathode for sodium-ion batteries, *Adv. Mater.* 27 (2015) 5895–5900.
- [36] H. Li, T. Jin, X. Chen, Y. Lai, Z. Zhang, W. Bao, L. Jiao, Rational Architecture Design Enables Superior Na Storage in Greener $\text{NaSICON-Na}_4\text{MnV}(\text{PO}_4)_3$ Cathode, *Adv. Energy Mater.* 8 (2018) 1801418.
- [37] X. Chen, K. Du, Y. Lai, G. Shang, H. Li, Z. Xiao, Y. Chen, J. Li, Z. Zhang, In-situ carbon-coated $\text{Na}_2\text{FeP}_2\text{O}_7$ anchored in three-dimensional reduced graphene oxide framework as a durable and high-rate sodium-ion battery cathode, *J. Power Sources* 357 (2017) 164–172.
- [38] C.S. Park, H. Kim, R.A. Shakoor, E. Yang, S.Y. Lim, R. Kahraman, Y. Jung, J.W. Choi, Anomalous manganese activation of a pyrophosphate cathode in sodium ion batteries: a combined experimental and theoretical study, *J. Am. Chem. Soc.* 135 (2013) 2787–2792.
- [39] J. Kim, I. Park, H. Kim, K.Y. Park, Y.U. Park, K. Kang, Tailoring a New 4V-Class Cathode Material for Na-Ion Batteries, *Adv. Energy Mater.* 6 (2016) 1502147.
- [40] P. Barpanda, G. Oyama, S. Nishimura, S.C. Chung, A. Yamada, A 3.8-V earth-abundant sodium battery electrode, *Nat. Commun.* 5 (2014) 4358.
- [41] D. Wang, X. Bie, Q. Fu, D. Dixon, N. Bramnik, Y.S. Hu, F. Fauth, Y. Wei, H. Ehrenberg, G. Chen, F. Du, Sodium vanadium titanium phosphate electrode for symmetric sodium-ion batteries with high power and long lifespan, *Nat. Commun.* 8 (2017) 15888.
- [42] E.a. Iffer, M. Belaiche, C.A. Ferdi, M. Elansary, A.K. Sunar, Y. Wang, Y. Cao, Monoclinic $\alpha\text{-NaVOPO}_4$ as cathode materials for sodium-ions batteries: Experimental and DFT investigation, *Int. J. Energy Res.* 45 (2020) 1703–1719.
- [43] P. Hu, X. Wang, T. Wang, L. Chen, J. Ma, Q. Kong, S. Shi, G. Cui, Boron Substituted $\text{Na}_3\text{V}_2(\text{P}_{1-x}\text{B}_x\text{O}_4)_3$ Cathode Materials with Enhanced Performance for Sodium-Ion Batteries, *Adv. Sci.* 3 (2016) 1600112.
- [44] J. Zhang, Y. Lai, P. Li, Y. Wang, F. Zhong, X. Feng, W. Chen, J. Liu, X. Ai, H. Yang, Y. Cao, Boosting rate and cycling performance of K-doped $\text{Na}_3\text{V}_2(\text{PO}_4)_2\text{F}_3$ cathode for high-energy-density sodium-ion batteries, *Green Energy Environ.* (2021), doi:10.1016/j.gee.2021.01.001.
- [45] M. Chen, L. Chen, Z. Hu, Q. Liu, B. Zhang, Y. Hu, Q. Gu, J.L. Wang, L.Z. Wang, X. Guo, S.L. Chou, S.X. Dou, Carbon-Coated $\text{Na}_3.32\text{Fe}_{2.34}(\text{P}_2\text{O}_7)_2$ Cathode Material for High-Rate and Long-Life Sodium-Ion Batteries, *Adv. Mater.* 29 (2017) 1605535.
- [46] C. Zhao, F. Ding, Y. Lu, L. Chen, Y.S. Hu, *Angew. Chem. Int. Ed.* 59 (2020) 264–269.
- [47] Y. Fang, J. Zhang, L. Xiao, X. Ai, Y. Cao, H. Yang, Phosphate Framework Electrode Materials for Sodium Ion Batteries, *Adv. Sci.* 4 (2017) 1600392.